References

BELOV, N. V., NERONOVA, N. N. & SMIRNOVA, T. S. (1955). *Tr. Inst. Kristallogr. Akad. Nauk SSSR*, **2**, 33-67.

BELOV, N. V., NERONOVA, N. N. & SMIRNOVA, T. S. (1957). *Kristallografiya*, **2**, 315-325.

JABLAN, S. (1984). *Publ. Inst. Math.* **36** (50), 35-44.

JABLAN, S. V. (1986*a*). *Acta Cryst.* A**42**, 209-212.

JABLAN, S. (1986*b*). *Publ. Inst. Math.* In the press.

ZAMORZAEV, A. M. (1957). *Kristallografiya*, **2**, 15-20.

ZAMORZAEV, A. M. (1962). *Kristallografiya*, **7**, 813-821.

ZAMORZAEV, A. M. (1963). *Kristallografiya*, **8**, 307-312.

ZAMORZAEV, A. M. (1976). *The Theory of Simple and Multiple Antisymmetry*. Kishinev: Shtiintsa.

ZAMORZAEV, A. M. & PALISTRANT, A. F. (1964). *Kristallografiya*, **9**, 778-782.

ZAMORZAEV, A. M. & PALISTRANT, A. F. (1980). *Z. Kristallogr.* **151**, 231-248.

ZAMORZAEV, A. M., PALISTRANT, A. F. & GALJARSKI, E. I. (1978). *Colored Symmetry, its Generalizations and Applications*. Kishinev: Shtiintsa.

Acta Cryst. (1987). A**43**, 337-346

Electron-Microscope Imaging of Short-Range Order in Disordered Alloys

BY N. TANAKA* AND J. M. COWLEY

Department of Physics, Arizona State University, Tempe, AZ 85287, *USA*

(*Received* 13 *March* 1985; *accepted* 11 *November* 1986)

Abstract

Dynamical diffraction effects of diffuse scattering due to point defects in crystals and the associated imaging are studied in relation to imaging of the short-range order in disordered alloys through theoretical formulations and computer image simulations. Simulations of gold crystals including one point defect without strain show that the image contrast is localized in atomic size and relatively insensitive to the defect depth when the total thickness is fixed. The contrast from a small number of defects in an atomic column can be simply related to the number of defects by a nonlinear expression. An approximate imaging theory for short-range order in disordered binary alloys is discussed. The present study shows that the important parameters for observations of defective crystals are total thickness and microscope defocus, but not the defect depth. With controlled values of these parameters and sample conditions, the images of disordered binary alloys can be interpreted semi-quantitatively.

1. Introduction

Electron-microscope observations of short-range order (SRO) in disordered alloys have been performed with diffuse scattering in the dark-field (Yamaguchi, Watanabe & Ogawa, 1961; Ruedl, Delavignette & Amelinckx, 1968; Chevalier & Stobbs, 1979) and bright-field (Dutkiewicz & Thomas, 1975) imaging modes. In the dark-field images, bright speckles about 2 nm in size were observed in various disordered alloys, which suggested small ordered domains. In the dark-field lattice images taken under conditions of diffuse scattering and fundamental reflections, the image features suggested localized ordered structures in a disordered matrix (Van Tendeloo, De Ridder & Amelinckx, 1978; Tanaka, Ohshima, Harada & Mihama, 1979). In the bright-field lattice images taken under conditions of direct wave and diffuse scattering, localized ordered regions were clearly observed with localized lattice-like fringes in disordered Cu–Pd (Tanaka & Ohshima, 1984; Van Tendeloo & Amelinckx, 1983) and Au–Mn alloys (Tanaka, Cowley & Ohshima, 1987).

The basis of image interpretation for disordered crystals in dark and bright fields is not sufficiently well established to allow analysis of the localized structures. The bright speckles in the dark-field images do not always correspond to single ordered domains (Cowley, 1973). The image features in the dark-field lattice images do not give correct information on atomic structures even for two-dimensional ordered alloys (Terasaki, Wood & Watanabe, 1984). In the axial bright-field images the overlap problem has to be clarified in the imaging theories and simulations.

In high-resolution electron microscopy of disordered or defective crystals, methods of intuitive image interpretation have to be sought, even though they are admitted to be just a first approximation. The standard method for the structure analysis, namely comparison between actual images and simulated ones, is not applicable to disordered crystals without starting models. A useful approximation for intuitive image interpretation is the weak-phase-object approximation, which is applicable to thin samples composed of light atoms. Other useful

* Present address: Department of Applied Physics, Faculty of Engineering, Nagoya University, Nagoya 464, Japan.

0108-7673/87/030337-10$01.50

approximations are the phase-grating approximation (Cowley, 1975) and the strong-phase-object approximation (Fejes, 1977), where the image contrast is not linearly related to the projected potential. The approximations are not directly applicable to the interpretation of most disordered alloys.

In the present paper, the image characteristics of point-defect structures are studied with simple models and image simulations in relation to the imaging of disordered crystals with SRO, especially for previous observations of disordered Au–15at.%Mn alloys (Tanaka, Cowley & Ohshima, 1987). The empirical fact that high-resolution electron-microscope images of point defects without strain are relatively insensitive to the depth of the defects is verified by multi-slice calculations and approximate imaging theories. The result is used to formulate an approximate imaging theory for the SRO state in disordered binary alloys.

2. Approximate imaging theories for point-defect structures

Crystals with localized defects such as point defects and substitutional atoms or SRO can be formulated in terms of an average periodic lattice and positive and negative deviations from the average lattice as illustrated in Fig. 1 (Cowley, 1981). In the multi-slice formulation, the projected potential of an atomic slice may be separated into the average periodic projected potential and the projected deviation. The transmission function for the ith slice can be written as

$$q_i(x) = \exp i\sigma[\bar{\varphi}_i(x) + \Delta\varphi_i(x)], \qquad (1)$$

where σ is the interaction constant ($=\pi/\lambda E$), $\bar{\varphi}_i$ is the projected potential due to an average lattice and $\Delta\varphi_i$ is that due to the deviation by defects or substitutional atoms. In reciprocal space the above transmission function is written as

$$\begin{aligned} Q_i(u) &= \hat{F}[q_i(x)] = \bar{Q}_i(u) * [\delta(u) + \Delta Q_i(u)] \\ \bar{Q}_i(u) &= \hat{F}[\exp i\sigma\bar{\varphi}_i(x)] \\ \Delta Q_i(u) &= \hat{F}\{\Delta q_i(x)\} = \hat{F}[\exp i\sigma\Delta\varphi_i(x) - 1], \end{aligned} \qquad (2)$$

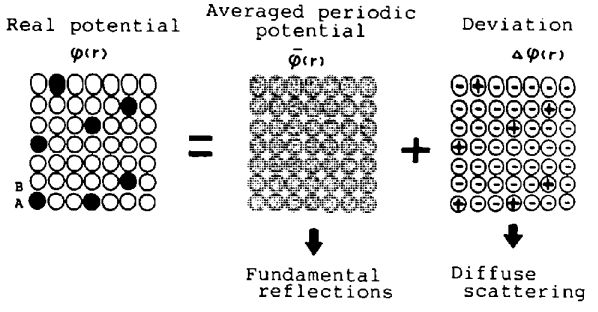

Fig. 1. Description of defective crystals or disordered binary alloys. + and − represent positive and negative deviations from the average periodic-lattice potential. The diffuse scattering is caused by the deviations.

where $\bar{Q}_i$ relates to the fundamental reflections from the average periodic lattice, ΔQ_i is concerned with the diffuse scattering from the deviations, and $\hat{F}$ and * denote two-dimensional Fourier transform and convolution, respectively. The wave function after the nth slice can be written as

$$\Psi_n(u) = [\Psi_{n-1}(u) \times P_n(u)] * Q_n(u), \qquad (3)$$

where P is the propagation function of the nth slice.

In the first approximation double and higher-order diffraction of the diffuse scattering may be neglected (Spence, 1978). The formulation including higher-order terms becomes too complicated for intuitive image interpretation in electron microscopy (Cowley & Fields, 1979). Under the 'single-diffraction approximation' the wave function after the Nth slice with deviations can be written as

$$\begin{aligned} \Psi_N(u) = {} & \bar{\Psi}_N(u) \\ & + \Psi_0(u)P_1(u) * \bar{Q}_1(u) * \Delta Q_1(u)P_2(u) \cdots P_N(u) * \bar{Q}_N(u) \\ & + \Psi_0(u)P_1(u) * \bar{Q}_1(u)P_2(u) \\ & \qquad * \bar{Q}_2(u) * \Delta Q_2(u)P_3(u) \cdots P_N(u) * \bar{Q}_N(u) \\ & \vdots \\ & + \Psi_0(u)P_1(u) * \bar{Q}_1(u)P_2(u) \cdots \bar{Q}_N(u) * \Delta Q_N(u) \end{aligned} \qquad (4)$$

where $\bar{\Psi}_N$ and Ψ_0 are the wave functions due to fundamental reflections and incident wave, respectively. The approximation may be reasonable when the wave field after a single diffuse scattering process is very weak and ΔQ_i is much smaller than $\bar{Q}_i$.

Each row except for the first in (4) represents a single diffuse scattering process by the deviation ΔQ_i. We need discuss only one row because the total wave function due to the diffuse scattering is the sum of the rows. In other words, multiple defects in an atomic column are treated independently in this approximation. The process consists of three parts: (i) the incident beam undergoes n-beam dynamical diffraction by the average lattice above the defect, (ii) the Bragg waves create the diffuse scattering at the ith slice and (iii) the diffuse scattering undergoes n-beam dynamical diffraction due to the average lattice below the defect layer (Cowley, 1981). The process is represented in real space as

$$\psi_j^d(x) = \bar{\psi}_j(x) \times [\exp i\sigma\Delta\varphi_j(x) - 1] \times [\bar{\psi}_{N-j}(x)], \qquad (5)$$

where $\bar{\psi}_j$ and ψ_j^d are wave functions of fundamental reflections and diffuse scattering due to a defect, respectively, and suffix j denotes the slice with the defect. The notation '$\times[\bar{\psi}_{N-j}(x)]$' is not a simple scalar product, but a multi-slice operation. The term does not strictly commute with the phase-grating term, $[\exp i\sigma\Delta\varphi_j(x) - 1]$.

Provided that the commutation does not drastically change the wave function $\psi_j^d(x)$, a point defect at a slice could be approximately shifted to the top or

bottom of the slice sequence and the following equation obtained from (4):

$$I(x)=|\bar{\psi}_N(x)+\bar{\psi}_N(x)\times\sum_j[\exp i\sigma\Delta\varphi_j(x)-1]|^2. \quad (6)$$

This equation gives an approximate projection of the three-dimensional distribution of defects in electron-microscope images. The approximation is useful for the image interpretation of disordered samples, although the relation between the image intensity and projected density of defects may be nonlinear. It should be noted that the commutation may to some extent cause a difference in phase, so the approximate similarity is mainly concerned with the image intensity as the result. In the image with lens aberration, the phase difference may cause a contrast difference.

In the limiting case where the diffracted waves do not spread so much in the lateral direction, as in the atomic column approximation (*e.g.* Howie & Basinski, 1969; Van Dyck, Van Tendeloo & Amelinckx, 1982), the propagation function can be neglected in the multi-slice sequence as

$$\psi_j^d(x)=\psi_0(x)\times q_1(x)\times q_2(x)\times\cdots \times q_j(x)\times\Delta q_j(x)\times\cdots\times q_N(x), \quad (7)$$

where the Δq_j can be moved to any position to get the same result in this case. The total wave field is written from (4) as

$$\begin{aligned}\psi(x)&=\psi_0\exp i\sigma\sum_i\bar{\varphi}_i(x)+[\psi_0\exp i\sigma\sum_i\bar{\varphi}_i(x)]\\&\quad\times\sum_j[\exp i\sigma\Delta\varphi_j(x)-1]\\&=\psi_0\exp i\sigma\sum_i\bar{\varphi}_i(x)[(1-N)+\sum_j\exp i\sigma\Delta\varphi_j(x)]\\&\simeq\psi_0\exp i\sigma\sum_i\bar{\varphi}_i(x)[1+\sum_j i\sigma\Delta\varphi_j(x)]. \quad (8)\end{aligned}$$

A similar formula can be derived from the phase-grating approximation as follows:

$$\begin{aligned}\psi(x)&=\psi_0\exp i\sigma\sum_i[\bar{\varphi}_i(x)+\Delta\varphi_i(x)]\\&=\psi_0\exp i\sigma\sum_i\bar{\varphi}_i(x)\times\exp i\sigma\sum_j\Delta\varphi_j(x)\\&=\psi_0\exp i\sigma\sum_i\bar{\varphi}_i(x)[1+i\sigma\sum_i\Delta\varphi_i(x)]. \quad (9)\end{aligned}$$

The validity of the phase-grating approximation has recently been discussed in terms of the tight binding of Bloch waves (Marks, 1986).

3. Image simulations of point-defect structures

3.1. *Models and simulation methods*

A simple model is used for clarifying diffraction phenomena in crystals with defects or deviations. The model is composed of $2\times2\times1$ f.c.c. units of gold or other atoms with point defects at arbitrary lattice points as shown in Fig. 2(*a*). The use of gold has to do with the image interpretation of disordered Au–15at.%Mn alloys (Tanaka, Cowley & Ohshima, 1987). Sequences of the phase gratings produced from the $2\times2\times0{\cdot}5$ unit of the model (slice thickness = 0·2 nm) may represent three-dimensional crystals with several point defects as illustrated in Fig. 2(*b*). Provided that the point defects are changed to other atoms as positive or negative deviations, the model can be related to the SRO in disordered binary alloys (see Fig. 1). The nearer the atomic numbers of the constituent atoms are, the weaker is the deviation.

The multi-slice image simulations were fully dynamically performed at accelerating voltages of 200 and 400 kV using a program with the second-order contrast transfer function of Ishizuka (1980). The number of waves included was 64×64 for most cases, which was determined from saturation of the accuracy. The absorption effect of electrons in crystals was not taken into account in the calculations. The size effect responsible for another kind of diffuse scattering (*e.g.* Warren, 1969) was not considered because the origins of SRO diffuse scattering were clarified in the present study. All the images hereinafter are bright-field images.

3.2. *Aberration-free images of a single point defect*

Fig. 3 shows aberration-free bright-field simulated images (the approximate intensity distribution of electrons below crystals) of gold crystals with a point defect shown by the arrows (see Fig. 2*a*), the electron incidence being along the [001] direction. The accelerating voltage is 400 kV. The images are formed

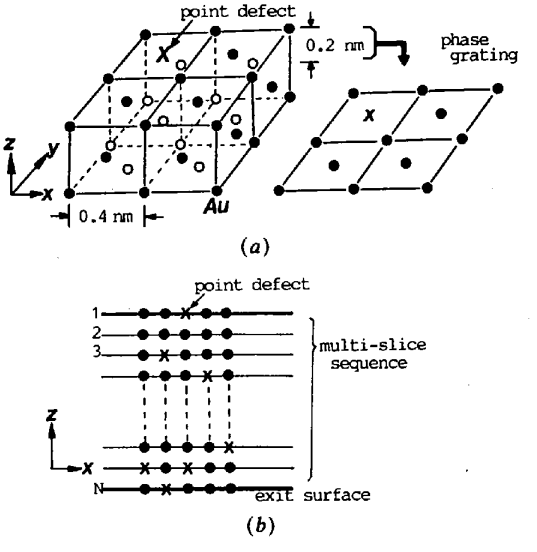

Fig. 2. (*a*) Model unit for multi-slice simulations. (*b*) Sequence of phase gratings produced from the unit represents three-dimensional crystals with point defects.

with all the scattering up to the 220 fundamental reflections for total thicknesses of 5·6 (28 slices), 8·8, 10·4 and 11·2 nm. The extinction distances of the 200 and 220 reflections for [001] axial incidence at 400 kV are 5·1 and 5·9 nm, respectively (see Fig. 4). The actual thickness can be obtained by multiplying the slice number by 0·2 nm. The figures below each result in Fig. 3 indicate the slice numbers of the defect layer compared with the number of slices in the total thickness given on the right-hand side.

The simulated images show that the effect of the point defect on the wave intensity below the crystal is confined to an area of less than 0·4 nm in diameter in all conditions. This is also confirmed by the simulated images formed with only diffuse scattering inside the 200 reflections (see Fig. 7*a*). This may be interpreted in terms of the atomic column approximation based on the channeling effect. The model unit with 2×2 unit mesh in Fig. 2(*a*) may thus be enough to simulate the diffraction phenomena in the crystal with point defects. There is little difference in the image contrast (intensity) due to the point defect between different defect depths as indicated by arrows. Figs. 4(*a*) and (*b*) show diffraction amplitudes and phases in two crystals where a point defect is located at the 13th or 19th slices. When the total thickness is fixed, the amplitudes and phases of the 100, 110 and 210 waves as diffuse scattering exhibit similarities between the two crystals. This explains the above insensitivity of the image contrast to the defect depth.

The simulated images for various defect depths have shown that the effect of one point defect on the wave intensity below the crystal is, if anything, relatively strong when the point defect is located at the depth where fundamental reflections, such as 200 and 220, are strong. This is because the wave field in the crystal, as Bloch waves, is changing from strong to weak enough to detect the existence of the point defect as illustrated in Fig. 5 (Fujimoto, 1978). It is noted that defects at top surfaces are not sensitively detected. The difference of the effect, however, does not drastically change the image features as shown in Fig. 3. The images show an approximate projection of the three-dimensional arrangements of point defects located in different atomic columns parallel to the observing direction. It has been checked that tilted illumination destroys the present simple image features with defect depth.

For a total thickness of 44 slices ($t=8{\cdot}8$ nm) in Fig. 3, there is little difference between the defect and non-defect cases. This is because the amplitudes of the 200 and 220 waves are so strong as to cover the effect of the point defect for the total thickness. The existence of suitable sample thicknesses for observing the effect of SRO diffuse scattering has been detected in actual electron-microscope images of disordered $LiFeO_2$ (Tanaka & Cowley, 1986). The result can be explained in terms of extinction of the direct beam, fundamental reflection and diffuse scattering.

The above point defect is the extreme case of negative deviation from the average lattice. The simulation

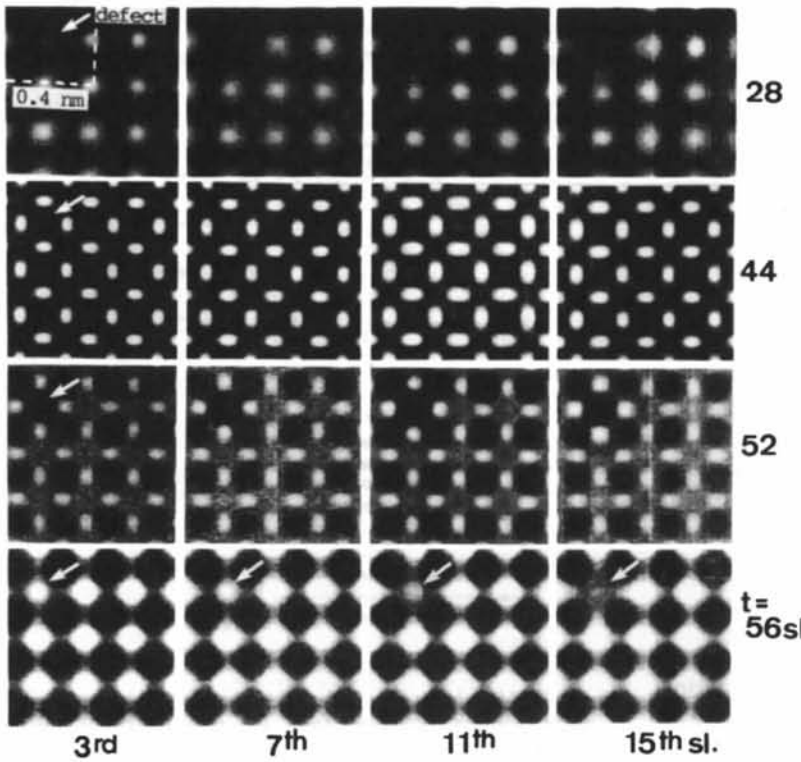

Fig. 3. Aberration-free bright-field stimulated images of gold crystals with one point defect at indicated depths (slice numbers below) at an accelerating voltage of 400 kV. The actual thickness can be calculated from multiplying the number of slices, given on the right hand side, by 0·2 nm.

of a gold crystal including a thorium single atom as the positive deviation has shown a little excess contrast on the lattice image of gold, which is opposite to that in Fig. 3. In disordered binary alloys, the deviations are much weaker than these cases, as explained in Fig. 1 and later. The effect of point deviations can thus be detected when they are accumulated over various image disturbances such as surface roughness and contamination.

3.3. *Two point defects separated horizontally*

Figs. 6(*a*) and (*b*) show aberration-free simulated images of two point defects separated horizontally (perpendicular to the electron beam) by 0·28 nm in the same slice (*a*) and separated horizontally in projection by 0·2 nm in different slices (*b*). In Fig. 6(*a*) a pair of defects are located at the ninth, 15th and 21st slices, the total thickness being fixed at 56 slices. The images of the paired defects appear separately and the image features do not change drastically with the defect depth. The image characteristic is similar for other total thicknesses. The results are consistent with the former case of one point defect in Fig. 3; the effect due to one point defect is confined to a small region less than 0·2 nm in half-width and the image contrast is relatively insensitive to the defect depth. In Fig. 6(*b*), when two defects are also separated in the z ([001]) direction as indicated by white numbers and a defect is located at the depth where the Bragg waves are relatively weak, the contrast of the paired defects becomes unbalanced as shown in the result for defects at the 15th and 40th slices. This result can be explained in a similar way to Fig. 5.

3.4. *Several point defects located in an atomic column*

Fig. 7(*a*) shows similar simulated images of several point defects located in an atomic column in gold

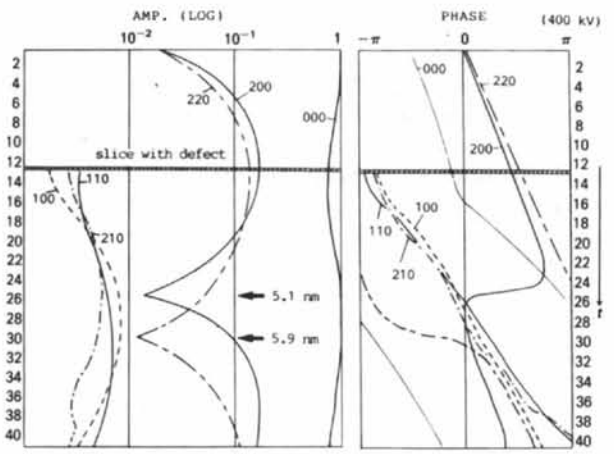

Fig. 4. Diffraction amplitudes and phases below two crystals with different defect depths, at the 13th and 19th slices.

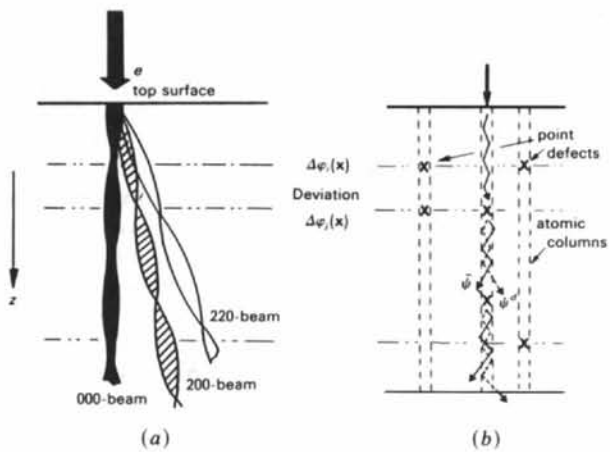

Fig. 5. (*a*) Illustration of behavior of diffracted waves in crystals and (*b*) atomic column approximation for imaging of point defects. $\bar{\psi}$ and ψ^d are waves of fundamental reflections and diffuse scattering, respectively.

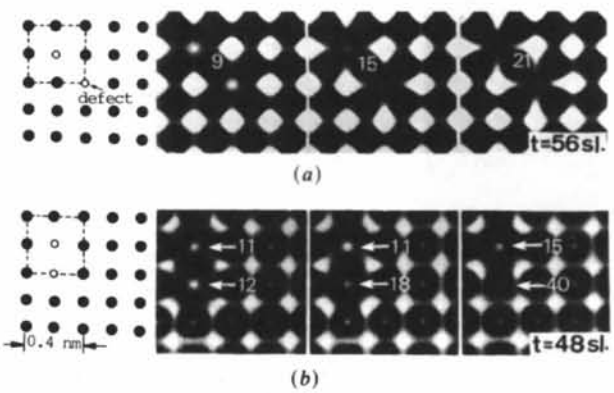

Fig. 6. Aberration-free simulated images of gold crystals with two point defects (*a*) separated horizontally by 0·28 nm and (*b*) separated in projection horizontally by 0·2 nm. White figures show the depth of point defects (slice numbers) and the total thicknesses are 48 and 56 slices, respectively.

crystals, the total thicknesses being 36 and 56 slices. The images are formed with the direct wave and diffuse scattering inside the 200 fundamental reflections in order to clarify the effect on the image contrast. The results for various cases have shown that the image contrast increases simply with the small number of defects, and the contrast does not drastically change with defect depth. Fig. 7(*b*) shows the relation between the image contrast and the number of defects in an atomic column for a total thickness of 56 slices. The contrast is defined as the difference of the peak intensity at the defect position from unity. The relation is nonlinear with saturation of the contrast around 10% at seven point defects. The contrast for more than seven point defects shows a complicated relation with the number of the defects, because the arrangement with many defects cannot be treated as a perturbation to the average periodic lattice owing to the dynamical interaction of diffuse scattering. When the density of defects is small, the contrast may thus be related to the richness. In a first approximation with neglect of double diffraction of diffuse scattering, the image contrast below crystals with several defects in an atomic column may be connected to a weighted sum of the effects due to each point defect, with extinction of Bragg waves taken into consideration as shown in Fig. 5. The reason for the low contrast is that the images are non-aberrated ones. Lens aberration adds to some extent to the phase contrast as shown later in Fig. 8.

In disordered binary alloys the deviation potential is much weaker than that due to the point defect. The simple relation between the image contrast and the number of deviations may extend to more than ten deviations in the abscissa. The calculated results for Mn atoms in gold crystals are shown by open circles in Fig. 7(*b*). For disordered Au–15at.% Mn alloys the number of minority Mn atoms in one atomic column is on average less than ten for a total thickness of 10 nm, which can be estimated from the computer reconstruction of the SRO state (Ohshima, Matsui, Harada & Adachi, 1986). The above result may be usable in the image interpretation (Tanaka, Cowley & Ohshima, 1987).

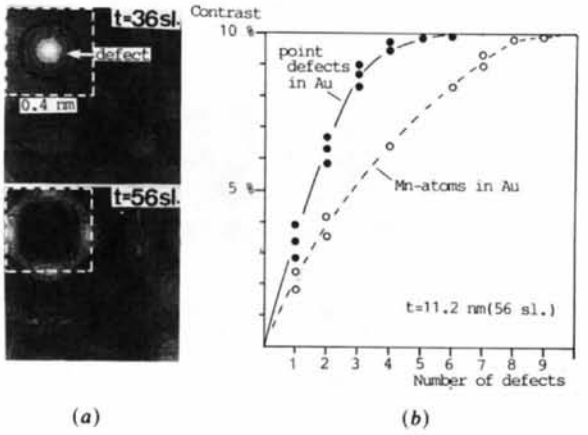

Fig. 7. (*a*) Aberration-free simulated images of a gold crystal with three point defects in an atomic column formed with the direct wave and diffuse scattering. (*b*) Relation between image contrast of point defects (filled circles) and Mn atoms (open circles) in an atomic column and the number of defects. Several points plotted at the same number represent cases with different defect depths.

3.5. *Simulated images with aberration and defocus*

In actual electron-microscope images, the effect of the contrast transfer function of the microscope has to be considered. The image contrast caused by either fundamental reflections or the diffuse scattering is affected more by the transfer function as well as the total thickness than by the effect of the difference of defect depth. The importance of lens defocus for imaging of point-defect clusters has already been pointed out by Rühle & Wilkens (1974). The transfer characteristic can be expressed for a thick object by the second-order total cross coefficient (O'Keefe, 1979; Ishizuka, 1980) rather than the linear contrast transfer function. Around the optimum defocus condition the image resolution is limited by the second-order envelope function. Provided that a microscope with point-to-point resolution less than 0·2 nm is used, the intensity variation for the gold crystals with point defects as shown in Figs. 3 and 6 can be reconstructed approximately in the image plane.

Fig. 8 shows bright-field image simulations of gold crystals with two point defects at the 13th and 14th slices as discussed in Fig. 6(*b*), the total thickness being 56 slices ($t = 11{\cdot}2$ nm). Two kinds of simulation parameters are used for microscopes with a point-to-point resolution of 0·18 nm (*A*) (accelerating voltage $E = 400$ kV; spherical aberration coefficient $C_s = 1{\cdot}0$ mm; energy spread $\Delta = 8$ nm; illumination half-angle $\beta = 5\times10^{-4}$ rad) and 0·23 nm (*B*) ($C_s = 4{\cdot}0$ mm, $\Delta = 10$ nm and $\beta = 5\times10^{-4}$ rad). Images (*a*) and (*c*) are simulated with all the scattering up to 220 reflections with microscopes *A* and *B*, respectively. The image (*b*) is formed with the direct wave and diffuse scattering inside the 200 fundamental reflections with microscope *A*. The image intensity shows clearly the existence of two localized point defects around the optimum defocus condition ($\Delta f \simeq -50$ nm) for the 'good' microscope (*A*) as shown by the arrows in Fig. 8(*a*). The images produced by microscope *B* show deblurring of the separation at the optimum defocus ($\Delta f \simeq -90$ nm) and misleading peaks of image intensity at other positions at a defocus of −150 nm, as indicated by the arrows in Fig. 8(*c*). The image contrast of the defects at the optimum defocus for each case (middle row) is calculated to be about (*a*) 20%, (*b*) 30% and (*c*) 25%. The insensitivity of the image contrast to defect depth has also

been confirmed in these aberrated images, in accordance with the results in Figs. 3 and 6, although the image contrast is reversed in some defocus conditions.

The reason why the 200 lattice fringes are not evident at the optimum defocus ($\Delta f \simeq -90$ nm) in Fig. 8(c) is that the contrast transfer characteristic for 200 spacing is depressed at the defocus condition. When the defocus is set at -150 nm (underfocus), the fringes become evident, but the 'image localization' (Marks, 1986) about localized defects may break down. The images formed with the direct wave and diffuse scattering can correctly show the existence of paired defects around the optimum defocus ($\Delta f \simeq -50$ nm) by the 'good' microscope (A) as shown in Fig. 8(b).

4. Imaging of the SRO state in binary alloys

With the above results and the single-diffraction approximation mentioned in § 2, the images of disordered alloys with SRO could be interpreted semi-quantitatively.

The average periodic potential for disordered binary alloys is written in a first approximation as

$$\bar{\varphi}(x) = \sum_K (C_A \varphi_A + C_B \varphi_B) * \delta(x - x_K) \qquad (10)$$

where $\varphi_{A/B}$ is the atomic potential of A or B atoms and $C_{A/B}$ is the mole fraction. The SRO diffuse scattering is caused by the two kinds of deviations from the above periodic potential at each lattice point (see Fig. 1):

$$\begin{aligned} \Delta\varphi_A(x) &= \varphi_A(x) - \bar{\varphi}(x) \quad (A \text{ atom occupied}) \\ \Delta\varphi_B(x) &= \varphi_B(x) - \bar{\varphi}(x) \quad (B \text{ atom occupied}), \end{aligned} \qquad (11)$$

where φ_A and φ_B for a lattice point can be determined approximately just by the occupation of A or B atoms at the lattice point. The validity of the approximation has been checked by the phase-grating calculation. The strain effect arising from the size difference of two constituent atoms is not taken into account in this formulation, which causes another kind of diffuse scattering.

In terms of the deviations $\Delta\varphi_A$ and $\Delta\varphi_B$, we may write the wave field below the disordered binary alloys under the single-scattering approximation as

$$\begin{aligned} \Psi_N(u) &\simeq \bar{\Psi}'_N(u) + n_A \Psi^d_A(u) + n_B \Psi^d_B(u) \qquad (12) \\ \Psi^d_{A/B} &= \bar{\Psi}_i * \Delta Q_{A/B} * (\bar{\Psi}_{N-i}) \\ \Delta Q_{A/B} &\rightleftharpoons \hat{F}(\exp i\sigma\Delta\varphi_{A/B} - 1), \end{aligned}$$

where $\bar{\Psi}'_N$ is the wave function due to the fundamental reflections a little attenuated by production of the diffuse scattering and $n_{A/B}$ is the number of A or B atoms. $\Psi^d_{A/B}$ is less sensitive to the depth of $\Delta Q_{A/B}$ as mentioned before. In this equation the apparently linear term $n_A \Psi^d_A$ has to be corrected using a relation such as that of Fig. 7(b) strictly. The image intensity in the ideal imaging condition can be written in real space as

$$\begin{aligned} I_N(x) \simeq & |\bar{\psi}_N(x)|^2 + 2\,\mathrm{Re}\,[n_A \psi^d_A(x) \bar{\psi}^*_N(x) \\ & + n_B \psi^d_B(x) \bar{\psi}^*_N(x)] \\ & + n_A^2 |\psi^d_A(x)|^2 + n_B^2 |\psi^d_B(x)|^2 \\ & + (\text{cross terms}), \end{aligned} \qquad (13)$$

where the first term is the lattice image due to the fundamental reflections including the dark-field-image intensity, the second term is the interference between the fundamental reflections (mainly direct wave) and the diffuse scattering and the third and fourth terms are the dark-field image due to the diffuse scattering.

In the bright-field images the image contrast of defects may be formed mainly by the second interference terms. The contrast is determined by the extinction of the direct wave and the diffuse scattering propagating in the lower crystals after the defects. A key point is that the variations in the amplitudes and phases of the fundamental reflections are dependent on the total sample thickness, but to a smaller extent on the depth of defects, when the number of defects is small. Furthermore, the extinction distance for the diffuse scattering is longer than those of the Bragg waves. The above interference terms are thus chiefly determined by the extinction of the fundamental reflections affected by the total thickness.

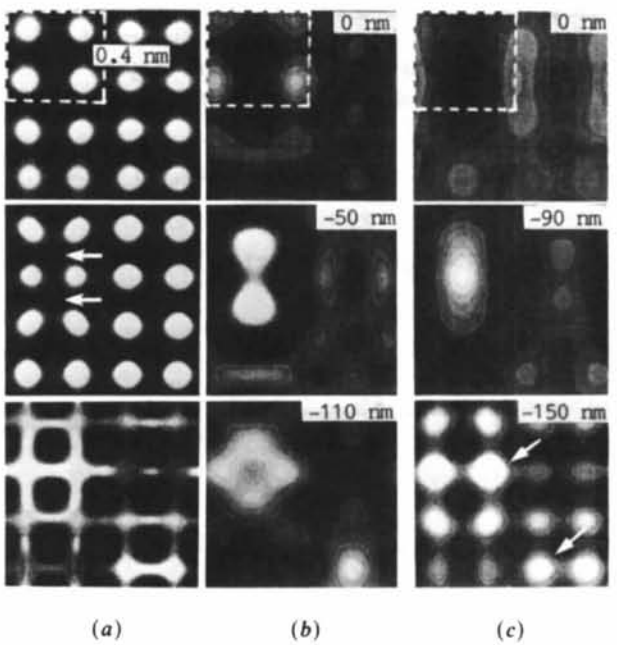

Fig. 8. Simulated through-focus images with aberration and defocus of a gold crystal with two point defects for a 400 kV microscope: (a) with all the scattering up to 220 reflections by microscope A; (b) with only diffuse scattering inside 200 reflections; and (c) with the same conditions as (a) by microscope B.

Fig. 9 shows simulated images of a hypothetical $L1_2$ ordered unit of Au_3Mn floating in a disordered f.c.c. matrix as illustrated in the attached schema for a 400 kV microscope. The contrast of the unit changes with the total sample thickness (t), but only slightly with the depth of the unit. The black contrast can be interpreted as positive deviations in suitable thicknesses ($t = 16$ nm; 40 slices), which can be predicted by multi-slice calculations. The result shows the possibility of observing small ordered domains in disordered alloys. In practice, it should be taken into account that fluctuation in disorder matrices may cause a noise-like contrast.

5. Discussion

The effect of strain owing to the size difference of atoms is neglected in the present simulations. The reason is that the strain gives another kind of diffuse scattering from that of SRO (Warren, 1969), and the diffuse scattering can be separated quantitatively from that of the SRO in X-ray diffuse scattering analysis (Borie & Sparks, 1971). The origin of the SRO diffuse scattering in the lattice occupancy has been clarified by the present simulations. Diffuse scattering from point defects with or without strain has been discussed in detail by Dederichs (1973). Calculations of image contrast of single vacancies related to stacking-fault tetrahedra with strain have recently been performed for gold crystals (Ajika, Hashimoto & Takai, 1985). It is essential for electron microscopy of disordered crystals to select the samples where the SRO diffuse scattering is sufficiently stronger than other diffuse scattering, which can be checked by X-ray diffuse-scattering analysis. Otherwise, images formed with the other diffuse scattering may give a misleading image contrast for analyzing the local structures.

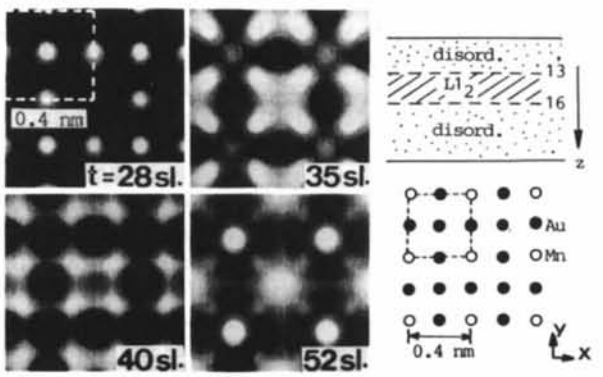

Fig. 9. Image simulations with aberration ($C_s = 1{\cdot}0$ mm) and defocus ($\Delta f = -48$ nm) of a small ordered $L1_2$ crystal of Au_3Mn sandwiched with two disordered f.c.c. crystals for a 400 kV microscope. This is a hypothetical model for the SRO in disordered Au–15at.%Mn alloys under the single-diffraction approximation. The actual thickness can be estimated from multiplying the slice number by 0·4 nm.

When the absorption effect in dynamical electron diffraction is included in the simulations, the essential results obtained here may not be changed, but the image contrast and extinction distances, which determine suitable observing thicknesses, may be changed to some extent. The reason why point defects are not easy to detect in actual high-resolution electron micrographs may be that the contrast is too weak to observe over various surface disturbances rather than the absorption effect.

In the formulations of §§ 2 and 4, the double-diffraction effect of diffuse scattering is neglected. The present simulations show that point defects in different atomic columns separated by more than 0·4 nm could be approximately treated independently, because the diffuse scattering from single point defects is confined to around the size of channeling propagation along the zone axis. This kind of small lateral spread of high-energy electrons was calculated also by Coene, Van Dyck, Van Tendeloo & Van Landuyt (1985). The problem of double diffraction arises mainly for multiple point defects in an atomic column. The diffuse scattering from one defect is subject to double diffraction at another defect below it. The result in Fig. 7(b) shows a nonlinear relation between the image contrast and the number of defects. In the single-scattering approximation, the contrast may be related to a weighted sum of contrasts due to each point defect along the z direction, when the extinction of the fundamental waves is considered.

When the effect of the double diffraction is included, it has to be added into the estimate in the single-scattering approximation as illustrated in Fig. 10. The main part of the correction may be written for correlation of two point defects in an atomic column as

$$\psi_{k,l}^{dd}(x) = \bar{\psi}_{k-1}(x) * p(x)q_k(x)\Delta q_k(x) * p(x) \times \cdots q_l(x)\Delta q_l(x) \cdots q_N(x),$$
$$\psi_N(x) = \psi'_N(x) + \sum_j \psi_j^d(x) + \sum_{k,l} \psi_{k,l}^{dd}(x), \qquad (14)$$

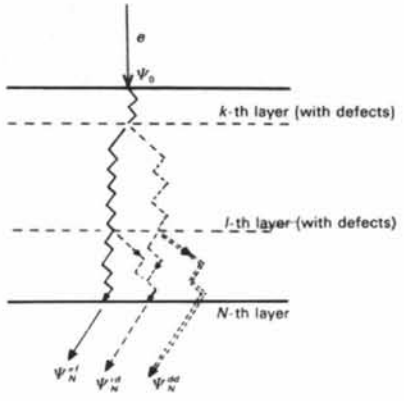

Fig. 10. Schematic description of double diffraction of diffuse scattering in defective crystals.

where ψ_{kl}^{dd} means double diffraction of diffuse scattering. The effect of Δq_k and Δq_l can be roughly estimated from (2) as

$$\Delta q_k \Delta q_l = [\exp i\sigma\Delta\varphi_k(x) - 1][\exp i\sigma\Delta\varphi_l(x) - 1]. \quad (15)$$

The term is estimated to be of third order, so the effect may be as small as the interference term in the previous first-order approximation (13). The simulation results have shown that the double-diffraction correction is less than 10% for typical diffuse scattering for gold crystals with two point defects. The amplitudes of waves below the crystals have to be reduced a little from (4). For gold crystals with Mn atoms, the correction becomes about 5% to support the single-diffraction approximation. When defects are many and arranged periodically along the z direction, they become a kind of ordered phase, which may cause dynamical diffraction effects in the diffuse scattering. This is similar to the case for two-dimensional ordered structures where the superstructure reflections are dynamical except for selected conditions (Shindo, 1982).

For large ordered regions, overlapping with other ordered regions strongly affects the image contrast (Kuwano, Hamada, Manabe & Eguchi, 1984). The present formulation can be applied to the 'diluted' case of ordered regions. The approximation has another implication that the incident wave into defective layers is only that from the fundamental reflections. The simulation in Fig. 9 is effective for the image interpretations of disordered alloys under the approximation; a disordered matrix with fluctuation can be replaced with an f.c.c. matrix of an average atom determined by the mole fraction. In practice, the fluctuation gives a weak noise-like contrast, which may be a disturbance to detect small ordered regions.

In the lattice images formed with fundamental reflections and diffuse scattering, the image contrast is mainly determined by the lattice fringes due to the fundamental reflections, which covers the effect of the diffuse scattering in some cases. Micrographs at the thicknesses where the lattice fringes are not so strong could be used for structure analysis of the SRO state. The image features showing the effect of diffuse scattering are sensitively changed through extinction of Bragg waves determined by the total thickness, as mentioned in § 4. The increase of accelerating voltage which makes the extinction distance short is not advantageous at that point, although the channeling effect becomes dominant, which makes the phase-grating approximation effective.

As shown in the present results, the wave field below crystals could show relatively correct local information about the SRO state in the form of a nonlinear projection with resolution around 0·2–0·3 nm; the disturbance usually occurs at the microscope lens. Since the image feature is strongly dominated by the lattice fringes of fundamental reflections, the microscope may require point-to-point resolution of down to 0·2 nm for gold crystals with point-defect structures or SRO. Otherwise, complicated 'trial and error' matching between actual images and the simulated images is required, which is less certain in most cases.

Actual high-resolution images are also disturbed by phase contrast owing to surface roughness and contamination, which is one of the important problems, as well as irradiation damage, in solving local atomic structures in high-resolution electron microscopy.

6. Concluding remarks

In the present simulations we can interpret the image contrast of disordered binary alloys with an image resolution around 0·2–0·3 nm in more detail than before. The channeling effect as a result of dynamical diffraction makes the formulation simple – the wave field below the crystals can be approximately treated independently at each atomic column. Because the modulation of the fundamental reflection is small and each diffuse scattering is very weak, the final wave field may be a sum of waves due to each point defect in the first approximation. The contrast of defects is nonlinearly related to the number of defects when the density of defects is small ('diluted' alloys). The geometry of the SRO state may be detected in the form of a nonlinear projection which shows the relative richness of one kind of atom in selected conditions. Estimates of extinction distances of the fundamental reflections and the image contrast of one point deviation are required to obtain suitable thicknesses before actual observations are made, as well as for checking the resolution of the microscope.

The present study was supported by NSF grant DMR7926460 and was performed using the facility for high-resolution electron microscopy at Arizona State University. The image simulations were carried out by a program in the facility prepared by Dr K. Ishizuka.

References

AJIKA, N., HASHIMOTO, H. & TAKAI, Y. (1985). *Phys. Status Solidi A*, **87**, 235–252.
BORIE, B. & SPARKS, C. J. (1971). *Acta Cryst.* **A27**, 198–201.
CHEVALIER, J. P. & STOBBS, W. M. (1979). *Acta Metall.* **27**, 285–289.
COENE, W., VAN DYCK, D., VAN TENDELOO, G. & VAN LANDUYT, J. (1985). *Philos. Mag.* **A52**, 127–143.
COWLEY, J. M. (1973). *Acta Cryst.* **A29**, 537–546.
COWLEY, J. M. (1975). Proc. 4th Int. Conf. High Voltage Electron Microscopy, Toulouse, pp. 129–134.
COWLEY, J. M. (1981). *Diffraction Physics*, 2nd ed. Amsterdam: North-Holland.
COWLEY, J. M. & FIELDS, P. M. (1979). *Acta Cryst.* **A35**, 28–37.
DEDERICHS, P. H. (1973). *J. Phys. E*, **3**, 471–496.
DUTKIEWICZ, J. & THOMAS, G. (1975). *Metall. Trans.* **6A**, 1919–1928.

FEJES, P. L. (1977). *Acta Cryst.* A**33**, 109-113.
FUJIMOTO, F. (1978). *Phys. Status Solidi A*, **45**, 99-106.
HOWIE, A. & BASINSKI, Z. S. (1969). *Philos. Mag.* **149**, 1039-1063.
ISHIZUKA, K. (1980). *Ultramicroscopy*, **5**, 55-65.
KUWANO, N., HAMADA, Y., MANABE, T. & EGUCHI, T. (1984). *J. Electron Microsc.* **33**, 335-343.
MARKS, L. D. (1986). *Ultramicroscopy*, **18**, 33-38.
OHSHIMA, K., MATSUI, M., HARADA, J. & ADACHI, K. (1986). *J. Magn. Mater.* **54-57**, 157-158.
O'KEEFE, N. A. (1979). *37th Ann. Proc. EMSA*, edited by G. W. BAILEY, pp. 556-567. Baton Rouge: Claitor.
RUEDL, E., DELAVIGNETTE, P. & AMELINCKX, S. (1968). *Phys. Status Solidi*, **28**, 305-328.
RÜHLE, M. & WILKENS, M. (1974). *J. Appl. Cryst.* **8**, 223-224.
SHINDO, D. (1982). *Acta Cryst.* A**38**, 310-317.
SPENCE, J. C. H. (1978). *Acta Cryst.* A**34**, 112-116.
TANAKA, N. & COWLEY, J. M. (1986). *Ultramicroscopy*, **17**, 365-378.
TANAKA, N., COWLEY, J. M. & OHSHIMA, K. (1987). *Acta Cryst.* B**43**, 41-48.
TANAKA, N. & OHSHIMA, K. (1984). *Phys. Status Solidi A*, **81**, 129-138.
TANAKA, N., OHSHIMA, K., HARADA, J. & MIHAMA, K. (1979). Proc. Mod. Str. Conf., Hawaii, pp. 292-294.
TERASAKI, O., WOOD, G. J. & WATANABE, D. (1984). *Proc. Mater. Res. Soc. Symp.* **21**, 253-257.
VAN DYCK, D., VAN TENDELOO, G. & AMELINCKX, S. (1982). *Ultramicroscopy*, **10**, 263-280.
VAN TENDELOO, G. & AMELINCKX, S. (1983). *Phys. Status Solidi A*, **77**, K9-K11.
VAN TENDELOO, G., DE RIDDER, R. & AMELINCKX, S. (1978). *Phys. Status Solidi A*, **49**, 655-666.
WARREN, B. E. (1969). *X-ray Diffraction*. Reading, MA: Addison-Wesley.
YAMAGUCHI, S., WATANABE, D. & OGAWA, S. (1961). *J. Phys. Soc. Jpn*, **17**, 1030-1041.

Acta Cryst. (1987). A**43**, 346-361

The Structure Determination of a Common Cold Virus, Human Rhinovirus 14

BY EDWARD ARNOLD, GERRIT VRIEND,* MING LUO, JAMES P. GRIFFITH, GREG KAMER, JOHN W. ERICKSON,† JOHN E. JOHNSON AND MICHAEL G. ROSSMANN

Department of Biological Sciences, Purdue University, West Lafayette, Indiana 47907, *USA*

(*Received* 21 *May* 1986; *accepted* 12 *November* 1986)

Abstract

The methods used to solve the structure of human rhinovirus 14 at 3·0 Å resolution are described in detail. The crystals are cubic, space group $P2_13$, a = 445·1 Å with 20-fold non-crystallographic redundancy and with approximately 55% solvent and RNA content. The data used to solve the structure were collected at the Cornell High Energy Synchrotron Source (CHESS) using oscillation photography. Most of the computations were performed on Purdue University's Cyber 205 supercomputer. Two heavy-atom derivative data sets from crystals soaked in 1 and 5 m*M* $KAu(CN)_2$ were used to provide isomorphous phasing to 4 Å resolution, although it was subsequently shown that phases beyond 5 Å resolution were random. The phases were refined at 5 Å resolution by five cycles of real-space molecular replacement. Phase extension from 5 to 3 Å was then performed using 60 cycles of real-space molecular replacement while extending the resolution in steps of three reciprocal-lattice points at a time once every three cycles. The 3·5 Å skew-averaged map was easily interpreted and showed 811 of the 855 amino acids in the four distinct viral polypeptide chains. A complete atomic model has been built using *FRODO* on an Evans & Sutherland PS300 graphics system with respect to the 3·08 Å resolution electron density map. The roles of the non-crystallographic symmetry, solvent content, errors in amplitudes, orientation and translation in the molecular replacement process are discussed.

Introduction

The earlier successful determinations of the small RNA plant viruses tomato bushy stunt virus (TBSV; Harrison, Olson, Schutt, Winkler & Bricogne, 1978), southern bean mosaic virus (SBMV; Abad-Zapatero, Abdel-Meguid, Johnson, Leslie, Rayment, Rossmann, Suck & Tsukihara, 1980) and satellite tobacco necrosis virus (STNV; Liljas, Unge, Jones, Fridborg, Lövgren, Skoglund & Strandberg, 1982) represented the largest molecular analyses by crystallographic techniques prior to the determination of two animal virus structures (Rossmann, Arnold, Erickson, Frankenberger, Griffith, Hecht, Johnson, Kamer, Luo, Mosser, Rueckert, Sherry & Vriend, 1985; Hogle, Chow & Filman, 1985). The plant virus structures not only laid the technological foundations but also provided a structural framework on which the subsequent work on animal viruses could be based. The major

* Present address: Department of Structural Chemistry, University of Groningen, Nijenborgh 16, 9747 AG Groningen, The Netherlands.

† Present address: Department of Physical Biochemistry, AP-9A D-47E, Abbott Laboratories, Abbott Park, North Chicago, Illinois 60064, USA.

0108-7673/87/030346-16$01.50